



# Retinal Vasculature Extraction using Non-Subsampled Contourlet Transform and Multi-structure Element Morphology by Reconstruction

Anil Kumar K.R, Meenakshy K.

**Abstract:** Retinal vasculature extraction is an area of utmost interest in ophthalmology. It helps to diagnose various diseases and also play a crucial role in treatment planning and accomplishment. In this work, we suggest an algorithm to segment retinal vasculature from retinal Fundus Images (FI) using multi-structure element morphology after enhancing the image using Normal Inverse Gaussian (NIG) model in the fuzzi-fied Non-Subsampled Contourlet Transform (NSCT) domain. Since both noises and weak edges produce low magnitude NSCT coefficients, image enhancement methods amplify weak edges as well as noises. Direct application of image boosting technique in the NSCT domain causes over enhancement. So a novel image enhancement method is employed by interpreting the term "contrast" as a qualitative instead of a quantitative measure of the image. Membership values of NSCT coefficients are modified using NIG model. Mathematical Morphology (MM) by Multi-structure Elements (MEs) is used to extract the edges of image. False vessel ridges are expunged, and the thin vessel edges are preserved using opening by reconstruction. Connected component analysis followed by length filtering is used to filter the still remaining false edges. In most of the available literature, low-resolution fundus image databases are used for evaluating the algorithm. In our work, we evaluate our algorithm not only utilizing the DRIVE database, a low-resolution retinal image (RI) database, but also using an openly available High-Resolution Fundus (HRF) image database. Our result illustrates that the proposed method outperforms the other techniques considered with average accuracy (ACC) of 96.71%. In addition to ACC, we also use F1-Score and Mathews Correlation Coefficient (MCC) to evaluate our method. The average values of the results obtained with the HRF image database for F1-Score and MCC are 0.8172 and 0.8031, respectively, which are very much encouraging.

**Index Terms:** Vessel Segmentation, Multi-structure Element Morphology by Reconstruction, Non Subsampled Contourlet Transform, Normal Inverse Gaussian Model

**Revised Manuscript Received on 30 July 2019.**

\* Correspondence Author

**Anil Kumar K.R\***, Assistant Professor, Department of Electronics and Communication Engineering, NSS College of Engineering, Palakkad, Kerala, India. (Research Scholar, University of Calicut)

**Dr. Meenakshy K**, Associate Professor, Department of Applied Electronics and Instrumentation Engineering, Government Engineering College, Kozhikode, Kerala, India

© The Authors. Published by Blue Eyes Intelligence Engineering and Sciences Publication (BEIESP). This is an [open access](https://creativecommons.org/licenses/by-nc-nd/4.0/) article under the CC-BY-NC-ND license [http://creativecommons.org/licenses/by-nc-nd/4.0/](https://creativecommons.org/licenses/by-nc-nd/4.0/).

## I. INTRODUCTION

Signs of hypertension, cardiovascular diseases, diabetes, stroke and arteriosclerosis can be identified by the inspection of the retinal vasculature. Automated segmentation and analysis of vasculature is the primary step towards development of an algorithm for automated assessment of various ophthalmologic diseases like arteriolar narrowing, diabetic retinopathy (DR), retinopathy in premature babies, the relationship between hypertensive retinopathy and vessel tortuosity and computer assisted laser surgery.

Considering the fact that various forms of image acquisition exists, it is necessary that segmentation methods must be independent of acquisition techniques. Even same modality images can show large variations depending on the patient, camera model, presence of pathologies, focus adjustments and illumination. These facts put forward the need of efficient preprocessing of fundus images before the development of segmentation algorithms so that the algorithms are independent on several parameter configurations.

## II. RELATED WORK

Ample research has been done to segment retinal blood vessels. Most innovative vessel extraction methods can be grouped into three categories (a) Machine learning, (b) Deformable Model and (c) Tracking methods.

Supervised and Unsupervised approaches are two kinds of machine learning method. Supervised technique is based on analyzing pixels of the image. Then a vessel or nonvessel label is assigned to it with the help of some rule inferred from labeled training sets. In [1] a comprehensive description and evaluation method centered on a completely connected discriminatively trained restricted random field technique is proposed for vessel separation from fundus image (FI). Radius-dependent Clustering ALgorithm (RACAL) is presented in [2] to fragment retinal vasculature in color photography. Neural network is applied in [3] to remove vessels of retina. Training is done with moment invariant and gray-level dependent features. Completely Convolutional Networks [4] are applied to part retinal vessels from FI. Cross-modality learning based segmentation is described in [5]. Here mapping function between vessel map and RI is learned by a deep neural network.



# Retinal Vasculature Extraction using Non-Subsampled Contourlet Transform and Multi-structure Element Morphology by Reconstruction

Lattice Neural Network is used in [6] along with Dendritic processing to segment out blood vessels. Unsupervised approaches are based on particular features derived from input's statistical distribution. By means of fuzzy C-means [7] extracts vessels from retinal images. By utilizing phase-congruency, non-uniform illumination problem is tackled. In [8], Particle Swarm Optimization is applied iteratively to optimize matched filter parameters.

An ant colony system based on a heuristic function is introduced in [9].

Deformable models consider surfaces inside the domain of image. These surfaces can move or deform when a force is exerted. Deformable model based methods can be categorized as region and edge based methods. Region-based techniques were first presented in [10]. Pixel intensity (to reduce false positive vessel) and local phase map (to obtain an accurate vessel map) are employed as region information in [11]. In [12], spatial constraints are put forward in the assessment of the local pixel strength distribution. An active B-snake contour is used in [13] to remove the blood vessel. But in the existence of pathology, the performance of [13] deteriorates.

Analysis based on tracking is restricted to local areas of the image. First, a reliable seed point is selected. Then identify centerlines of vessel by iteratively selecting the optimum candidate pixel. Minimum Cost Path (MCP) with key point detection [14] lets to improve the MCP robustness to noise.

The paper is structured as follows: Section III briefs the NSCT. Fuzzy logic is presented in Section IV. Mathematical morphology is introduced in Section V. There after the proposed method is explained in Section VI. Illustration and evaluation of our experimental results are presented in Section VII. Conclusions are summed up in Section VIII.

## III. NON-SUBSAMPLED CONTOURLETS AND FILTER BANKS

An outline of the NSCT described in [15] is displayed in Fig 1. NSCT is made up of two non-subsampled shift-invariant portions

- i. pyramid structure
- and
- ii. Directional Filter Bank structure (DFB).

The first guarantees the multi-scale characteristics and the second brings directionality.

### III.1 Non-Subsampled Pyramid (NSP)

Fig 2 reveals the NSP breakdown with  $J = 3$  stages with  $J + 1$  redundancy where,  $J$  is the number of breakdown stages.  $H_1(z) = H_0(z) - 1$  where  $H_0(z)$  represents low-pass filter. The regions  $[-\frac{\pi}{2^j}, \frac{\pi}{2^j}]^2$  and  $[-\frac{\pi}{2^{j-1}}, \frac{\pi}{2^{j-1}}]^2 / [-\frac{\pi}{2^j}, \frac{\pi}{2^j}]^2$  are the theoretical pass band of the low pass as well as high pass filters respectively at the  $J^{th}$  step. The subsequent stage filters are

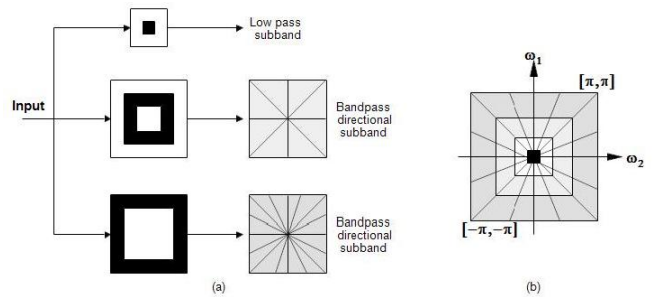


**Fig1: NSCT. (a) NSF arrangement to form the NSCT. (b) Idealized frequency splitting achieved using the recommended structure. Source [15]**

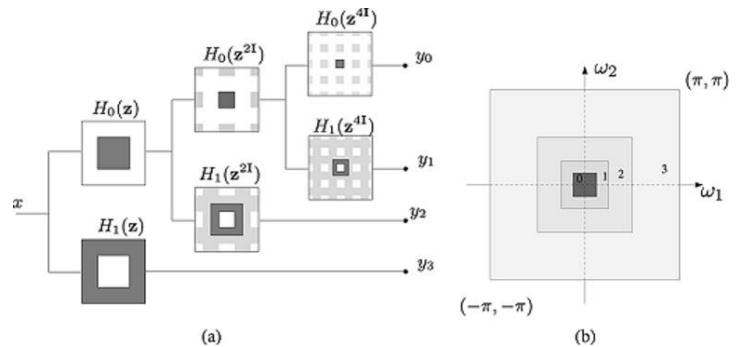


**Fig 2:(a) 3-stagenon-subsampled pyramid breakdown. (b) Subbands on the 2-D frequency plane. Source [15]**

obtained by upsampling the first stage filters. This results a  $J + 1$  redundancy [15].

## III.2 Non-Subsampled Directional Filter Bank(NSDFB)

NSDFB is built by turning off both the down/up samplers in the 2-channel filter bank in the DFB tree assembly and accordingly the filters are upsampled. Fig 3 illustrate a 4-channel decomposition. The process of merging the NSP and NSDFB to construct NSCT produce severe aliasing in the higher stages of the pyramid unless the NSDFB filters are judiciously upsampled. A  $J -$  level NSCT is performed on image  $I$  resulting low frequency sub-band coefficients  $C_{j0}^J(p, q)$  at the  $j^{th}$  scale and band pass sub-band coefficients  $C_{j,l}^J(p, q)$  in the  $j^{th}$  scale and on the  $l^{th}$  direction. Here  $(p, q)$  represents the location.

## IV. FUZZY SETS

L.A Zadeh introduced fuzzy set theory. A fuzzy set, as described in (1), is an ordered pair consisting of elements and a corresponding membership function that assigns a membership value to each element.

$$A = \{(z, m_A(z)) | z \in Z\} \quad (1)$$

where,  $Z$  is the universe of discourse, and  $m_A(z)$  is the membership value of element  $z$  in the fuzzy set  $A$ , which can take a value in the interval  $[0, 1]$ .

Let  $I(p, q) | p, q \in \mathbb{R}^2$  be a digital image of size  $M \times N$

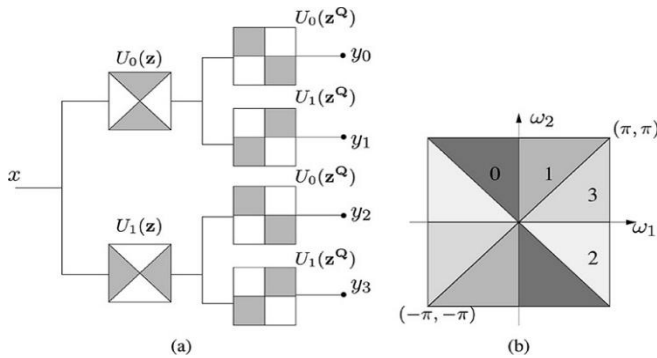


Fig 3: 4-channel NSDFB constructed with 2-channel fan filter banks.

(a) Filtering assembly. (b) Equivalent frequency breakdown. Source [15]

with  $L$  gray levels extending from 0 to  $L - 1$ . Image  $I$  can be considered as a collection of fuzzy singletons. The elements of this array are the membership value,  $m_I(g_{pq})$ , of the gray level  $g_{pq}$ , corresponding to the  $(p, q)^{th}$  pixel, concerning to an image property such as homogeneity, edginess, brightness, etc. We consider the property "brightness" for image enhancement task. As per the fuzzy set notation, an image  $I$  can be represented as  $I = \left\{ \frac{m_I(g_{pq})}{g_{pq}} \mid p = 0, 1 \dots M - 1, q = 0, 1 \dots N - 1 \right\}$ . Fuzzy image enhancement involves of 3 sequential steps

1. Fuzzification
2. Modification of membership values using the following rules.
  - i. Modify *dark* pixels into *darker* pixels.
  - ii. Retain *gray* pixels as such.
  - iii. Modify *bright* pixels into *brighter* pixels.

3. Defuzzification.

### V. MATHEMATICAL MORPHOLOGY

Mathematical morphology, a useful technique for handling a variety of problems in image processing, is a group of morphological algebraic operations. Results of morphological operation largely based on the size as well as shape of Structuring Elements (SEs) and are, therefore, selected as per the requirement of the allied application.

In 2-dimensional Euclidean space  $\mathbb{R}^2$ , let  $I(p, q)$  represents a grayscale image. Let  $Se$  be a defined SE. The top-hat transformation described in (2) can be used to find edges of an image.

$$top - hat(I) = I - (I \circ Se) \quad (2)$$

where  $\circ$  denote the opening operator. The problem with the top-hat operator is that it contains all the tiny ordinary intensity variations. Moreover, this problem is severely aggravates due to irregular background illumination of the FI. The modified top-hat can be used to solve this problem [16]. In modified top-hat, the initial image is first subjected to morphological closing operation, and then a morphological

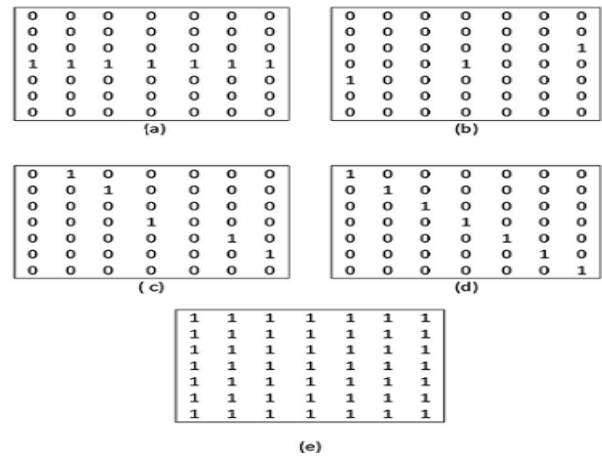


Fig 4:(a-d) Some of  $Se_i$  for  $N=3$  and directional resolution =  $15^\circ$ . (e)  $7 \times 7$  SE.

opening operation is performed on the result. By using a minimum operator, the effect of the morphological opening operation is compared to the original image to obtain an image identical to the original image apart in edges. The revised top-hat transformation [16] is defined by (3).

$$top - hat(I) = I - \min((I \bullet Se_c) \circ Se_o; I) \quad (3)$$

where  $Se_o$  and  $Se_c$  are the SEs for opening ( $\circ$ ) and closing ( $\bullet$ ) operators, respectively.

#### V.1 Multi-structure elements Morphology

To detect simple, ordinary, and straight edges of an image single and symmetrical SEs are used. But as the complexity of the edges increases, they fail to detect complex edges. For detecting such intricate edges, we require more advanced SEs. In multi-structure element morphology, we gather many SEs in a square window. Consequently, such SEs are capable of distinguishing edges with different directions, competently. An SE in  $(2N + 1) \times (2N + 1)$  window is denoted by (4) as below.

$$Se_i = I \left\{ (p + p_0, q + q_0), \phi_i = i \times \frac{180^\circ}{4N} \right\} \quad (4)$$

where  $\phi_i$  is the direction angles of  $Se_i$ ,  $-N \leq p_0, q_0 \leq N$  and  $i = 0, 1, \dots, 4N - 1$ . The dimension of the SE window is selected based on the required directional resolution. Fig 4(a-d) represents several  $Se_i$  for directional resolution =  $15^\circ$  and Fig 4(e) represents the  $7 \times 7$  SE constructed from the combination of all  $Se_i$  in all directions [16].

#### V.2 Morphological Operations by Reconstruction

Even though morphological opening and closing operations leave features higher than SEs unchanged, the key limitation of these operations is that they do not keep edge information safely and clearly. An operator named M- and N-sieves address this defect by emphasizing merely on the size of the features but without considering the shape. This problem is addressed by morphological operators by reconstruction by considering the shape and size of the features [16].

If we designate the mask and marker images with  $u$  and  $v$  respectively, the geodesic dilation of size 1 of  $v$  with respect to  $u$  is meant by  $\delta_u^{(1)}(v)$  and is the pointwise minimum ( $\wedge$ ) of the element dilation  $\delta^{(1)}$  of  $v$  and  $u$ .

$$\delta_u^{(1)}(v) = \delta^{(1)}(v) \wedge u \quad (5)$$

Likewise, the geodesic erosion  $\epsilon_u^{(1)}(v)$  is the point wise maximum ( $\vee$ ) of the element erosion  $\epsilon^{(1)}$  of  $v$  and  $u$ .

$$\epsilon_u^{(1)}(v) = \epsilon^{(1)}(v) \vee u \quad (6)$$

The geodesic dilation(erosion) of a particular size is obtained by carrying out continuous geodesic dilation(erosion) of  $v$  and  $u$ .

$$\delta_u^{(1)}(v) = \delta_u^{(1)}[\delta_u^{(i-1)}(v)] \quad (7)$$

$$\epsilon_u^{(1)}(v) = \epsilon_u^{(1)}[\epsilon_u^{(i-1)}(v)] \quad (8)$$

for  $i = 1, 2, 3 \dots$ ,  $\delta_u^{(0)}(v) = v$  and  $\epsilon_u^{(0)}(v) = v$ . Both (7) and (8) converge after several iterations, and remain unchanged after that. This steady state is the reconstruction by dilation and represented by (9)

$$\delta_u^{rec}(v) = \delta_u^n(v) \quad (9)$$

where  $n$  is such that  $\delta_u^n(v) = \delta_u^{(n+1)}(v)$ . Similarly, reconstruction by erosion is denoted by  $\epsilon_u^{rec}(v) = \epsilon_u^n(v)$  where  $n$  is such that  $\epsilon_u^n(v) = \epsilon_u^{(n+1)}(v)$ . So opening and closing by reconstruction are indicated by  $v \circ Se$  and  $v \bar{\circ} Se$  respectively and defined by (10) and (11) as

$$v \circ Se = \delta_u^{(rec)}(v \circ Se) \quad (10)$$

$$v \bar{\circ} Se = \epsilon_u^{(rec)}(v \bar{\circ} Se) \quad (11)$$

In summary, in its first step, morphological opening by reconstruction eliminates bright features that are smaller in size than the SE. In the second step, it brings back the outlines of components that have not been fully eliminated by opening by performing dilation operation iteratively and taking the original image as the reference. Closing by reconstruction is performed in case of features that are dark. Hence, the limitations of conventional morphological opening and closing operations, such as producing new edges, deforming the contours and edge drift, will not occur by employing opening and closing by reconstruction.

## VI. PROPOSED METHOD

Proposed algorithm is explained in detail in this section.

### VI.1 Image Channel Selection and Fundus Detection

The green component contrast of RGB retinal image is highest with the background. So it is selected to apply our algorithm. Otsu thresholding followed by morphological closing is performed to detect the fundus region. Application of NIG model based contrast enhancement in fuzzified NSCT domain results some artifacts external to the fundus region. These artifacts produce false edges during the edge detection stage. By using the fundus region mask these artifacts can be eliminated. It also saves the running time of the algorithm as our region of interest is now the area inside the fundus region.

### VI.2 Image Contrast Enhancement Using NSCT

The characteristics of NSCT make it perfect choice to successfully capture geometrical and directional features of the image. NSCT coefficient can be altered to enhance the image edges, thereby refining the image contrast. We interpret the term contrast as a qualitative measure. So fuzzy membership values of NSCT coefficients are found out by using (12) where  $C_{j,l}^J(p, q)$  is the NSCT coefficient corresponding to the  $(p, q)^{th}$  pixel in the  $J^{th}$  scale and on the  $l^{th}$  direction and  $C_{j,l}^{J(min)}$  and  $C_{j,l}^{J(max)}$  are the minimum and maximum values of NSCT coefficients in the  $J^{th}$  scale and on the  $l^{th}$  direction subband.

$$m_{j,l}^J(p, q) = \frac{C_{j,l}^J(p, q) - C_{j,l}^{J(min)}}{C_{j,l}^{J(max)} - C_{j,l}^{J(min)}} \quad (12)$$

The NSCT coefficients corresponding to smooth region of the image are approximately zero and those corresponding to edges are high in magnitude. Fig 5 shows the histogram distribution of the 3<sup>rd</sup> layer subband of NSCT coefficients in the 1<sup>st</sup> direction [17]. As evident from the Fig 5 the NIG probability density function (PDF) can accurately model the coefficient distribution.

We used (12) to find membership values of the NSCT coefficients so that the statistical characteristics of the NSCT coefficients are preserved in the fuzzified domain also. The key concern in the contrast enhancement problem is the optimization of threshold value which classifies image pixels into dark, gray and bright pixels. In this work we use NIG model to define the distribution of membership values of NSCT coefficients of an image. NIG PDF can be expressed by (13).

$$f_x(x) = \frac{\alpha \delta}{\pi q(x)} \cdot \exp [p(x)] \cdot K_1[\alpha q(x)] \quad (13)$$

where  $p(x) = \delta \sqrt{\alpha^2 - \beta^2} + \beta(x - \mu)$ ,  $q(x) = \sqrt{\delta^2 + (x^2 - \mu^2)}$  and  $K_1(\cdot)$

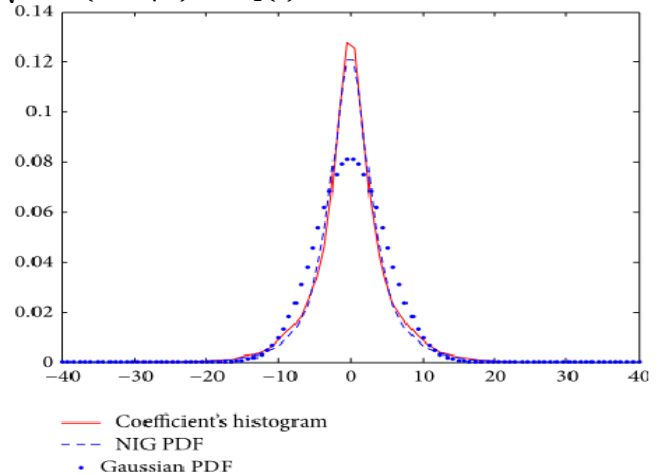


Fig 5: NSCT Probability density function corresponding to a particular subband of image with size 512 x 512 and NIG as well as Gaussian PDFs fitted to it. Source [17]

symbolizes a modified Bessel function of the 2<sup>nd</sup> kind with index 1. The parameters ( $\alpha, \beta, \mu, \delta$ ) determine the distribution of NIG. For most images, the decomposition coefficients are usually symmetrical distributions [17]. So  $\beta = \mu = 0$  is assumed so that the PDF corresponding to NIG can be simplified as (14).

$$f_x(x) = \frac{\alpha \delta \exp(\alpha \delta) K_1(\alpha \sqrt{x^2 + \delta^2})}{\pi \sqrt{x^2 + \delta^2}} \quad (14)$$

Using optimum linear interpolation between each coefficient and its corresponding subband mean Fathi and Naghsh-Nilchi[18] developed OLI-shrink algorithm. According to this algorithm modified membership value  $\bar{m}_{j,l}^J(p, q)$  can be obtained by(15).

$$\bar{m}_{j,l}^J(p, q) = \begin{cases} 0, & \text{if } |C_{j,l}^J(p, q)| \leq \lambda \\ \min((m_{j,l}^J(p, q) - \eta_m(m_{j,l}^J(p, q) - \mu_m)), & \\ & \text{if } |C_{j,l}^J(p, q)| > \lambda \end{cases} \quad (15)$$

where  $\mu_m$  is the mean of the membership values of the NSCT coefficients  $C_{j,l}^J$  of the corresponding subband and  $\eta_m$  can be obtained using  $\eta_m = \frac{\sigma_{nm}^2}{\sigma_m^2}$  where  $\sigma_m^2$  is the variance of membership values in the corresponding subband. The algorithm to find parameter  $\sigma_{nm}^2$  is given below.

1. Do orthogonal wavelet transform on the image and find noise standard deviation,  $\hat{\sigma}_n$ , using the robust median estimator (16)

$$\hat{\sigma}_n = \frac{\text{median}(|Y_{i,j}^{HH1}|)}{0.6745} \quad (16)$$

where  $Y_{i,j}^{HH1}$  is HH1 subband's coefficient.

2. Construct a white Gaussian noise image of size same as that of the original image and with zero mean and variance  $\hat{\sigma}_n^2$ .
3. Apply NSCT on the noisy image.
4. Find the membership values of these NSCT coefficients of noisy image using (12).
5. Obtain the variance  $\hat{\sigma}_{nm}^2(k)$  of membership values corresponding to each high frequency subband.
6. Go to step 2 and repeat the above steps 5 times. The final coefficient variance  $\sigma_{nm}^2$  is obtained by averaging the  $\hat{\sigma}_{nm}^2(k)$  obtained.

The threshold value  $\lambda$  is obtained by (17).

$$\lambda = \sigma_n^2 B \quad (17)$$

where  $\sigma_n$  is obtained in a similar way as explained above to find  $\sigma_{nm}^2$ . But here step 4 is not performed and so variances of the NSCT coefficients are calculated. Representing  $C_{j,l}^J(p, q)$  as  $C$

$$B = \left| \frac{2C}{\delta^2 + C^2} + \frac{\alpha C}{\sqrt{\delta^2 + C^2}} \cdot \frac{k_0(\alpha \sqrt{\delta^2 + C^2})}{k_1(\alpha \sqrt{\delta^2 + C^2})} \right| \quad (18)$$

$$\delta = \sqrt{\xi \times \hat{k}_2(1 - \rho^2)} \quad (19)$$

$$\alpha = \frac{\xi}{\delta(1 - \rho^2)} \quad (20)$$

$$\xi = 3 \left( \gamma_4 - \frac{4\gamma_3^2}{3} \right)^{-1} \quad (21)$$

$$\rho = \frac{\gamma_3 \sqrt{\xi}}{3} \quad (22)$$

where  $k_0(\bullet)$  and  $k_1(\bullet)$  are the modified Bessel function of 2<sup>nd</sup> kind with index 0 and 1 respectively,  $\gamma_3$  is the skewness and  $\gamma_4$  is the kurtosis of the NSCT coefficients.

$$\gamma_3 = \frac{\hat{k}_3}{(\hat{k}_2)^{3/2}} \quad (23)$$

$$\gamma_4 = \frac{\hat{k}_4}{(\hat{k}_2)^2} \quad (24)$$

where  $\hat{k}_1, \hat{k}_2, \hat{k}_3$  and  $\hat{k}_4$  are the 1 to 4 order cumulants of the NSCT coefficients respectively. Different directional subbands in NSCT shows different noise variance because of the nonorthogonal nature of NSCT [15]. After modifying the membership values using (15) an inverse transform is carried using (25) to obtain modified NSCT coefficients.

$$\bar{C}_{j,l}^J(p, q) = \bar{m}_{j,l}^J(p, q) \left[ C_{(j,l)max}^J - C_{j,l}^J(p, q) \right] + C_{(j,l)min}^J \quad (25)$$

Using modified NSCT coefficients reconstruct the enhanced image. The image augmentation steps described above are summarized below:

1. Accomplish NSCT to get a series of NSCT coefficients.
2. Find out the membership values of each subband coefficients using the (12).
3. Apply monte-carlo method to estimate the noise variance of each subband coefficients.
4. For each subband in each level compute the threshold value and statistical parameters of the coefficients as follows:
  - i. the terms  $\delta$  and  $\alpha$  using (19) and (20) respectively
  - ii. the threshold value  $\lambda$  using (17).
  - iii. the mean  $\mu$  and variance  $\sigma_c^2$  of each high frequency subbands.
  - iv. the term  $\eta$  using  $\eta \approx \frac{\sigma_n^2}{\sigma_c^2}$ .
5. Modify the membership values of all subbands using (15).
6. Perform defuzzification using (25) to obtain modified NSCT coefficients.

7. Perform the inverse NSCT to reconstruct the enhanced image.

The method described above boosts every weak edge in the image. This includes edges of thin vessels as well as feeble edges rising from uneven background illumination. So an image background is estimated by the opening morphology operator with a disk shaped structure element with radius above 15 pixels and is deducted from the improved image to nullify the uneven background illumination effect. Fig 6 shows the image before applying the proposed enhancement algorithm and image after applying the proposed enhancement algorithm.

### VI.3 Edge Detection Using Multi-structure Elements Morphology

The steps involved to detect retinal blood vessels can be summarized as below [16].

1. Produce the required SEs ( $Se_i$ ) to obtain the required directional resolution.
2. Obtain the subedge image  $F(I)_i$  of the original image by applying the chosen edge detector function  $F$  using the produced SEs in step 1 on the original image.
3. Accomplish the whole of the obtained edges using the (26).

$$F(I) = \sum_{i=0}^{M-1} W_i F(I)_i \quad (26)$$

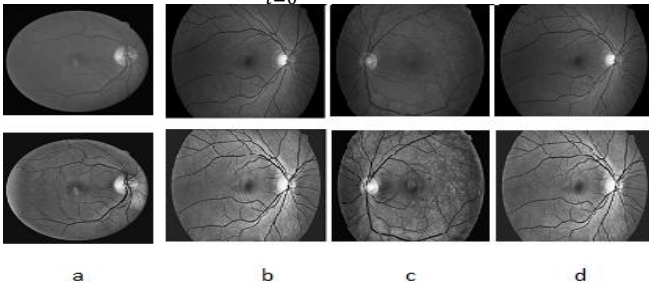


Fig 6: Result of proposed enhancement method. (a) is the result produced by image 25 of DRIVE database. (b)-(d) are result produced by image 01\_h, 01\_dr and 01\_g of HRF database correspondingly. First row is green channel images and second row is contrast enhanced images.

where  $F(I)$  is the total edge image,  $M = \frac{180}{\theta}$  and  $W_i$  is the allocated weight of subedge image. Defining the assigned weights as  $W_i = \frac{1}{M}$  will result the identical effect to each  $F(I)_i$ . We can also use (27) so that the larger  $F(I)_i$  has the better effect.

$$W_i = \frac{F(I)_i}{\sum_{i=0}^{M-1} F(I)_i} \quad (27)$$

False edges produced due to uneven background are eliminated in the subsequent steps.

### VI.4 False Edge Removal

Result of the morphological opening by reconstruction is enhanced by using MEs since MEs are extremely sensitive to boundaries in all directions. The SE employed here is identical to that in the edge detection step but with different

weight. Maximum  $F(I)_i$  is selected rather than assigning weights to each  $F(I)_i$  while constructing the  $F(I)_i$  so that weak false edges are prevented from contributing in construction of  $F(I)_i$ . Then reconstruction by dilation is performed with a flat SE. Since average width of blood vessel is 5 pixels, use of larger SEs for opening results removal more objects. Also it totally eliminates certain small vessels as they cannot be restored using reconstruction by dilation. Hence to attain a perfect final result without the presence of false edges we use adaptive connected component analysis.

### VI.5 Adaptive Connected Component Analysis (ACCA)

In ACCA we study images in distinct tiles and to each tile apply Connected Component Analysis (CCA) along with length filtering. Connected component pixels which are recognized above a particular threshold and labeled via 8 connected neighborhoods are treated as a single entity in CCA. After CCA, the components with length smaller than a particular threshold  $T$  are removed. The specific threshold can be obtained with a simple thresholding method and given by (28).

$$T = \mu - \alpha\sigma \quad (28)$$

where  $\mu$  is the mean,  $\sigma$  is the standard deviation and  $\alpha$  should be small enough ( $\alpha < 1$ ) for poor contrast images. Finally all the images are merged to a single image to obtain the final blood vessel detection result. Hence, the suggested blood vessel extraction algorithm includes the following steps.

1. Choose green component of original RGB image.
2. Get the fundus mask by Otsu thresholding and morphological closing
3. Apply NSCT
4. Find the membership values of the NSCT coefficients in each high frequency subband
5. Modify the membership values of NSCT coefficients
6. Using this modified membership values modify NSCT coefficients in each high frequency subband.
7. Rebuild the contrast boosted image using improved NSCT coefficients
8. Subtract the estimated background from the enhanced image
9. Perform the modified top-hat transform using the multi-structure elements morphology and get the edge image
10. Perform opening by reconstruction with MEs to eliminate the incorrect edges.
11. Apply ACCA to eliminate the still remaining false edges.

## VII. EXPERIMENTAL RESULTS

The algorithm summarized in Section VI.5 is applied to both DRIVE and HRF image database. MATLAB version 13 is used to implement our proposed method.

**VII.1 Implementation**

Since vessels perfectly stand out in green component, the algorithm proposed in Section VI is applied to these green channel images. Fundus region disk was formed in the next step. Afterward, perform NSCT to the green channel. Then the membership values of each NSCTsubband coefficients were obtained and modification function was applied to each of these membership values. Then using the modified membership values, obtain the modified NSCT coefficients. Apply the inverse NSCT to get the boosted image. The unwanted objects external to the fundus disc that result from enhancement step are removed by multiplying the boosted image with the diskfundus region. Then by improved top-hat using the multi-structure element morphology the edges of the image were identified. We used a  $7 \times 7$  SE with *directional resolution* =  $15^\circ$ . Then the incorrect edges are eliminated by morphological opening by reconstruction with MEs. ACCA is carried out to remove remaining false edges. Size of every block is found experimentally and is  $61 \times 61$ . Results produced in each phase are indicated in Fig 7.

**VII.2 Enhancement Assessment**

Several methods were available in the literature to assess the image contrast improvement. They fall into two classes. (i) Objective and (ii) Subjective. One of the objective measures is Peak Signal to Noise Ratio (PSNR). PSNR evaluates the intensity changes between the original and the enhanced image. Mean Square Error (MSE) and PSNR can be computed using (29) and (30).

$$MSE = \frac{1}{mn} \sum_{i=1}^m \sum_{j=1}^n \|I_0(i, j) - I_e(i, j)\|^2 \tag{29}$$

$$PSNR = 10 \log_{10} \left( \frac{255^2}{MSE} \right) \tag{30}$$

Another objective method to evaluate contrast enhancement is Contrast Improvement Index (CII) [16] that can be defined by (31).

$$CII = \frac{C_{en}}{C_{ori}} \tag{31}$$

where  $C_{en}$  and  $C_{ori}$  are the contrast of the boosted and original images respectively. The image contrast can be given by (32)

$$C = \frac{r - b}{r + b} \tag{32}$$

where  $b$  and  $r$  are the average grayscale value of the background and foreground, respectively. The results of assessment of proposed algorithm using the above mentioned measures are shown in Table (I)-(IV). Small values of standard deviations of PSNR and CII show good robustness of the method.

In subjective measures, help from human observers (such as ophthalmologist) are taken. They are requested to comment on edge details, presence of artifacts in the

enhanced image, similarity between the enhanced image and the original image.

**VII.3 Segmentation Assessment**

Recall or Sensitivity or True Positive Rate (TPR), False Positive Rate (FPR), PREcision (PRE), ACC, F1-Score and MCC are used to measure the algorithm performance. These measures can be defined as follows

$$TPR = \frac{TP}{TP + FN} \tag{33}$$

$$FPR = \frac{FP}{FP + TN} \tag{34}$$

$$ACC = \frac{TP + TN}{TP + FP + TN + FN} \tag{35}$$

$$PRE = \frac{TP}{TP + FP} \tag{36}$$

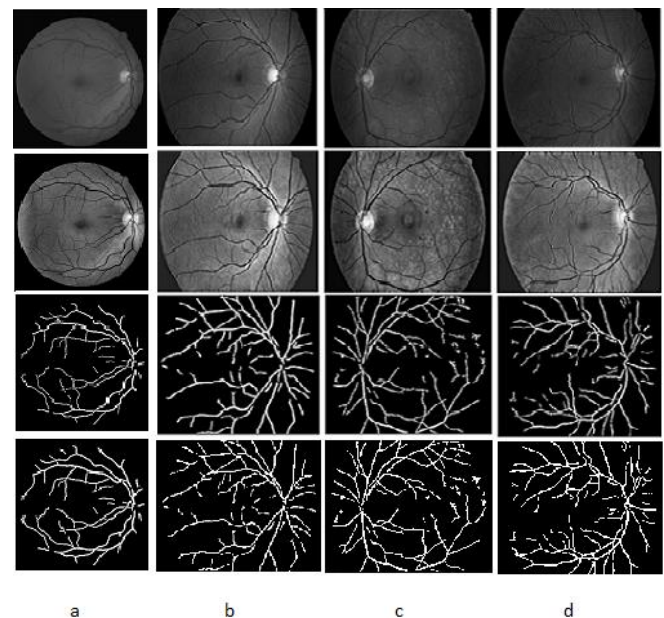


Fig 7: Result of suggested method. (a) is the result of proposed method to image 40 of DRIVE database. (b)-(d) are results produced images 01\_h, 01\_dr, 01\_g of HRF database, respectively. From top row to bottom row they are the green channel, contrast enhanced image, result before applying length filtering and last row are result after applying length filtering.

**Table I: Quantitative Assessment of Proposed Contrast Enhancement Method on DRIVE Database**

DRIVE Database		
Measure	Average	STD
PSNR	34.68	1.13
CII	1.36	0.004

**Table II: Quantitative Assessment of Proposed Contrast Enhancement Method on HRF\_h Database**

HRF_h Database		
Measure	Average	STD
PSNR	32.41	1.14
CII	1.28	0.012

**Table III: Quantitative Assessment of Proposed Contrast Enhancement Method on HRF\_dr Database**

HRF_dr Database		
Measure	Average	STD
PSNR	29.16	1.19
CII	1.27	0.037

**Table IV: Quantitative Assessment of Proposed Contrast Enhancement Method on HRF\_g Database**

HRF_g Database		
Measure	Average	STD
PSNR	31.72	1.16
CII	1.27	0.016

$$F1 - Score = \frac{2(Precision \times Recall)}{Precision + Recall} \quad (37)$$

$$MCC = \frac{TP \times TN - FP \times FN}{\sqrt{(TP + FP)(TP + FN)(TN + FP)(TN + FN)}} \quad (38)$$

where  $TP$  and  $TN$  are the blood vessel pixels and background pixels which are correctly detected respectively.  $FN$  (False Negative) is the pixels associated to a vessel, but is identified as background pixel mistakenly and  $FP$  (False Positive) shows the pixels not associated to a vessel, but is identified as blood vessel pixels.  $TP$  or recall indicates the capability of the method to well identify blood vessel. Probability of falsely recognizing a pixel as blood vessel pixel is  $FPR$ .  $ACC$  provides a general measure of the ratio of total well-detected pixels according to gold standard hand-labeled segmentation. When the cost of false positive is high, precision is a good measure. When a balance between precision and recall is needed  $F1$ -Score is a good option.  $MCC$  is more informative when compared to  $F1$ -Score and  $ACC$  in evaluating binary classification problems.  $F1$ -Score and  $ACC$  do not completely consider the size of the four classes of the confusion matrix in their final score calculation and hence they can be misleading. Table V displays the results obtained when algorithm is tested using DRIVE database. Performance comparison of our algorithm with others in terms of  $TPR$ ,  $FPR$  and  $ACC$  is illustrated in Table VI. It is illustrated in the Table VI that our method provides more  $ACC$  and  $TPR$  and lowest  $FPR$ . The proposed method was also assessed using HRF database. All the three sets of images-images of healthy eyes, images with signs of DR and glaucoma-were used. Tables VII-IX display results of the parameters  $TPR$ ,  $FPR$ ,  $ACC$ , Precision,  $F1$ -Score and  $MCC$  evaluated on particular datasets. Average values (Ave) and Standard Deviations (Std) were calculated for each parameter as well. The average values indicated at the bottom row reveals the robustness of our algorithm. A quantitative comparison of average values of  $ACC$ , show more than 96% of truly classified pixels in the field of vision for all datasets. The average values of  $F1$ -Score show that our algorithm maintains a relatively high balance between precision and recall. It can be observed from Table VII-IX that the  $MCC$

values are close to 1 which indicates that the proposed method fully considered the four classes of the confusion matrix. Table X compares performance of the proposed method with [19]. We only included  $SE$ ,  $FPR$  and  $ACC$  in Table X because [19] has not evaluated  $F1$ -Score and  $MCC$ . As Table X shows, our method is superior when compared with the other methods.

**Table V: Results obtained with DRIVE images.**

Im No	TPR	FPR	ACC	PRE	F1-Score	MCC
21	0.9429	0.0036	0.9922	0.9576	0.9502	0.9460
22	0.8825	0.0043	0.9854	0.9539	0.9168	0.9097
23	0.9049	0.0532	0.9436	0.5882	0.7130	0.7028
24	0.8861	0.0075	0.9805	0.9368	0.9107	0.9003
25	0.8512	0.0068	0.9805	0.9254	0.8868	0.8771
26	0.9621	0.0039	0.9933	0.9568	0.9594	0.9557
27	0.8622	0.0069	0.9814	0.9237	0.8919	0.8824
28	0.8509	0.0040	0.9817	0.9588	0.9016	0.8935
29	0.9374	0.0076	0.9877	0.9202	0.9287	0.9221
30	0.9551	0.0104	0.9868	0.8875	0.9201	0.9136
31	0.9721	0.0113	0.9876	0.8600	0.9126	0.908
32	0.9649	0.0073	0.9904	0.9227	0.9433	0.9383
33	0.9484	0.0048	0.9912	0.9486	0.9485	0.9437
34	0.8696	0.0274	0.9625	0.7755	0.8199	0.8006
35	0.9270	0.0076	0.9867	0.9214	0.9242	0.9169
36	0.8802	0.0108	0.9773	0.9087	0.8942	0.8816
37	0.9172	0.0067	0.9867	0.9297	0.9234	0.9161
38	0.9695	0.0182	0.9807	0.8352	0.8974	0.8898
39	0.9616	0.0168	0.9814	0.8450	0.8995	0.8916
40	0.9535	0.0101	0.9870	0.8922	0.9218	0.9154
<b>Ave</b>	<b>0.9200</b>	<b>0.0115</b>	<b>0.9822</b>	<b>0.8924</b>	<b>0.9032</b>	<b>0.8953</b>
<b>Std</b>	<b>0.0415</b>	<b>0.0111</b>	<b>0.0110</b>	<b>0.0839</b>	<b>0.0525</b>	<b>0.0547</b>

**Table VI: Comparison of Performance between Different Methods. Source [16]**

Method	TPR	FPR	ACC
Mendoca and Campilho	0.7344	0.0236	0.9452
Staal et.al.	0.6780	0.0170	0.9441
Martinez-Perez et.al.	0.7246	0.0345	0.9344
Niemeier et.al.	0.6898	0.0304	0.9416
Miri and Mahlooifar.	0.7352	0.0205	0.9458
<b>Our Method</b>	<b>0.9200</b>	<b>0.0115</b>	<b>0.9822</b>

**Table VII: Results obtained with HRF HEALTHY images.**

Im No	TPR	FPR	ACC	PRE	F1-Score	MCC
1	0.8732	0.0183	0.9706	0.8438	0.8582	0.8421
2	0.9409	0.0294	0.9677	0.7802	0.8530	0.8397
3	0.6234	0.0049	0.9556	0.9383	0.7491	0.7441
4	0.7647	0.0133	0.9556	0.8586	0.8089	0.7917
5	0.9430	0.0240	0.9729	0.7980	0.8645	0.8532
6	0.8928	0.0293	0.9627	0.7759	0.8303	0.8119
7	0.9057	0.0206	0.9728	0.8120	0.8563	0.8428
8	0.8446	0.0168	0.9692	0.8492	0.8469	0.8298
9	0.9571	0.0241	0.9744	0.7708	0.8539	0.8460
10	0.8431	0.0230	0.9654	0.7758	0.8081	0.7899
11	0.9480	0.0297	0.9682	0.7681	0.8486	0.8368
12	0.9127	0.0274	0.9663	0.7972	0.8510	0.8346
13	0.8288	0.0157	0.9706	0.8353	0.8320	0.8159
14	0.8180	0.0252	0.9610	0.7579	0.7868	0.7661
15	0.9748	0.0279	0.9723	0.7503	0.8479	0.8417
<b>Ave</b>	<b>0.8714</b>	<b>0.0220</b>	<b>0.9677</b>	<b>0.8074</b>	<b>0.8330</b>	<b>0.8191</b>
<b>Std</b>	<b>0.0880</b>	<b>0.0068</b>	<b>0.0049</b>	<b>0.0484</b>	<b>0.0310</b>	<b>0.0313</b>

**Table VIII: Results obtained with HRF DR images.**

Im No	TPR	FPR	ACC	PRE	F1-Score	MCC
1	0.9472	0.0286	0.9698	0.7031	0.8071	0.8014
2	0.8376	0.0168	0.9718	0.8094	0.8233	0.8081
3	0.8565	0.0473	0.9455	0.5975	0.7039	0.6882
4	0.8544	0.0360	0.9561	0.6485	0.7373	0.7220
5	0.8372	0.0130	0.9755	0.8423	0.8397	0.8265
6	0.6360	0.0012	0.9662	0.9810	0.7717	0.7750
7	0.7745	0.0165	0.9640	0.8280	0.8004	0.7812
8	0.8642	0.0479	0.9441	0.6434	0.7376	0.7168
9	0.7523	0.0071	0.9726	0.9068	0.8224	0.8118
10	0.7125	0.0145	0.9569	0.8518	0.7759	0.7560
11	0.7932	0.0201	0.9610	0.8158	0.8043	0.7828
12	0.8359	0.0218	0.9665	0.7748	0.8042	0.7866
13	0.8446	0.0170	0.9713	0.8208	0.8325	0.8170
14	0.8318	0.0303	0.9572	0.7322	0.7788	0.7571
15	0.8832	0.0287	0.9641	0.7312	0.8000	0.7847
<b>Ave</b>	<b>0.8174</b>	<b>0.0231</b>	<b>0.9628</b>	<b>0.7791</b>	<b>0.7893</b>	<b>0.7743</b>
<b>Std</b>	<b>0.0725</b>	<b>0.0130</b>	<b>0.0091</b>	<b>0.1005</b>	<b>0.0374</b>	<b>0.0386</b>

**Table IX: Results obtained with HRF GLUCOMA images.**

Im No	TPR	FPR	ACC	PRE	F1-Score	MCC
1	0.9501	0.0252	0.9729	0.7574	0.8429	0.8347
2	0.9097	0.0228	0.9716	0.7853	0.8429	0.8301
3	0.9252	0.0215	0.9748	0.7638	0.8368	0.8277
4	0.9216	0.0209	0.9747	0.7843	0.8474	0.8369
5	0.9368	0.0204	0.9763	0.7922	0.8585	0.8492
6	0.9321	0.0226	0.9738	0.7816	0.8502	0.8399
7	0.8873	0.0187	0.9741	0.7957	0.8390	0.8264
8	0.9095	0.0269	0.9681	0.7422	0.8174	0.8051
9	0.8959	0.0203	0.9733	0.7862	0.8375	0.8251
10	0.8751	0.0169	0.9748	0.8124	0.8426	0.8296
11	0.8384	0.0167	0.9705	0.8288	0.8336	0.8175
12	0.8485	0.0285	0.9600	0.7554	0.7992	0.7787
13	0.8207	0.0172	0.9698	0.8065	0.8135	0.7971
14	0.8448	0.0264	0.9628	0.7463	0.7925	0.7739
15	0.8263	0.0253	0.9621	0.7521	0.7875	0.7678
<b>Ave</b>	<b>0.8881</b>	<b>0.0220</b>	<b>0.9706</b>	<b>0.7793</b>	<b>0.8294</b>	<b>0.8160</b>
<b>Std</b>	<b>0.0417</b>	<b>0.0038</b>	<b>0.0050</b>	<b>0.0249</b>	<b>0.0213</b>	<b>0.0247</b>

**Table X: Comparison of our method with other blood vessel segmentation algorithm [19] evaluation on HRFDatabase**

	TPR	FPR	ACC
Our method (HRF-healthy images)	0.8714	0.0220	0.9677
Odstrcilik et.al. (HRF-healthy images)	0.7861	0.025	0.9539
Our method (HRF-DR images)	0.8174	0.0231	0.9628
Odstrcilik et .al.(HRF-DR images)	0.7463	0.0381	0.9445
Our method (HRF-Glaucoma images)	0.8881	0.0220	0.9706
Odstrcilik et.al.(HRF-Glaucoma images)	0.7900	0.0362	0.9497

**VIII. CONCLUSIONS**

In this work a technique for the retinal vessel extraction has been presented. Due to inherent properties of the retinal images detection of retinal vasculature is a very challenging procedure. Using modified NSCT coefficients contrast of RI was improved and equipped for extraction step. The NSCT coefficients are modified using fuzzy logic and NIG prior model whose parameters can be chosen compliantly and varied adaptively.



# Retinal Vasculature Extraction using Non-Subsampled Contourlet Transform and Multi-structure Element Morphology by Reconstruction

Advantage of NIG model is that it can precisely explain the high-pitch of the NSCT coefficients at zero and heavy tailed characteristics distributed symmetrically on either sides. So Bayesian method of denoising is employed for contrast enhancement of images. MEs morphology was used to identify blood vessels. Then morphological opening by reconstruction using MEs was applied to eradicate wrong edges. The remained false edges are removed by applying ACCA. Quantitative evaluation of both enhancement and segmentation algorithms illustrates that our method successfully identifies the blood vessels in low resolution and high resolution images with accuracy greater than 96%, F1-Score greater than 0.8 and MCC value greater than 0.77.

## ACKNOWLEDGEMENT

The authors express their gratitude to the Image Science Institute, University Medical Center Utrecht for making the DRIVE database publicly available. We would like to extend our thankfulness to Pattern Recognition Lab (CS5), the Department of Ophthalmology, Friedrich-Alexander University Erlangen-Nuremberg (Germany), and the Brno University of Technology, Faculty of Electrical Engineering and Communication, Department of Biomedical Engineering, Brno (Czech Republic) for providing HRF database. The authors are also thankful to Dr. Soman Nair, Specialist Ophthalmologist & Vitreoretinal Surgeon, Thumbay Hospital, Dubai, UAE for providing comment on edge details, presence of artifacts in the enhanced image, similarity between the enhanced image and the original image.

## REFERENCES

1. J. I. Orlando, E. Prokofyeva, and M. B. Blaschko, "A discriminatively trained fully connected conditional random field model for blood vessel segmentation in fundus images," *IEEE Transactions on Biomedical Engineering*, vol. 64, no. 1, pp. 16–27, 2017.
2. N. M. Salem, S. A. Salem, and A. K. Nandi, "Segmentation of retinal blood vessels based on analysis of the hessian matrix and clustering algorithm," in *2007 15th European Signal Processing Conference*. IEEE, 2007, pp. 428–432.
3. D. Marn, A. Aquino, M. E. Gegúndez-Arias, and J. M. Bravo, "A new supervised method for blood vessel segmentation in retinal images by using gray-level and moment invariants-based features," *IEEE Transactions on medical imaging*, vol. 30, no. 1, pp. 146–158, 2010.
4. A. Dasgupta and S. Singh, "A fully convolutional neural network based structured prediction approach towards the retinal vessel segmentation," in *2017 IEEE 14th International Symposium on Biomedical Imaging (ISBI 2017)*. IEEE, 2017, pp. 248–251.
5. Q. Li, B. Feng, L. Xie, P. Liang, H. Zhang, and T. Wang, "A cross-modality learning approach for vessel segmentation in retinal images," *IEEE transactions on medical imaging*, vol. 35, no. 1, pp. 109–118, 2015.
6. R. Vega, G. Sanchez-Ante, L. E. Falcon-Morales, H. Sossa, and E. Guevara, "Retinal vessel extraction using lattice neural networks with dendritic processing," *Computers in biology and medicine*, vol. 58, pp. 20–30, 2015.
7. T. Mapayi, J.-R. Tapamo, and S. Viriri, "Retinal vessel segmentation: a comparative study of fuzzy c-means and sum entropy information on phase congruency," *International Journal of Advanced Robotic Systems*, vol. 12, no. 9, p. 133, 2015.
8. K. Sreejini and V. Govindan, "Improved multiscale matched filter for retina vessel segmentation using pso algorithm," *Egyptian Informatics Journal*, vol. 16, no. 3, pp. 253–260, 2015.
9. A. H. Asad, A. T. Azar, and A. E. Hassani, "A new heuristic function of ant colony system for retinal vessel segmentation," in *Medical Imaging: Concepts, Methodologies, Tools, and Applications*. IGI Global, 2017, pp. 2063–2081.
10. T. F. Chan and L. A. Vese, "Active contours without edges," *IEEE Transactions on image processing*, vol. 10, no. 2, pp. 266–277, 2001.
11. Y. Zhao, L. Rada, K. Chen, S. P. Harding, and Y. Zheng, "Automated vessel segmentation using infinite perimeter active contour model with

- hybrid region information with application to retinal images," *IEEE transactions on medical imaging*, vol. 34, no. 9, pp. 1797–1807, 2015.
12. Z. Xiao, M. Adel, and S. Bourenane, "Bayesian method with spatial constraint for retinal vessel segmentation," *Computational and mathematical methods in medicine*, vol. 2013, 2013.
13. Y. Cheng, X. Hu, J. Wang, Y. Wang, and S. Tamura, "Accurate vessel segmentation with constrained b-snake," *IEEE Transactions on Image Processing*, vol. 24, no. 8, pp. 2440–2455, 2015.
14. V. Kaul, A. Yezzi, and Y. Tsai, "Detecting curves with unknown endpoints and arbitrary topology using minimal paths," *IEEE Transactions on Pattern Analysis and Machine Intelligence*, vol. 34, no. 10, pp. 1952–1965, 2011.
15. A. L. Da Cunha, J. Zhou, and M. N. Do, "The nonsubsampled contourlet transform: theory, design, and applications," *IEEE transactions on image processing*, vol. 15, no. 10, pp. 3089–3101, 2006.
16. M. S. Miri and A. Mahloojifar, "Retinal image analysis using curvelet transform and multistructure elements morphology by reconstruction," *IEEE Transactions on Biomedical Engineering*, vol. 58, no. 5, pp. 1183–1192, 2011.
17. J. Jia, Y. Zhang, L. Chen, and Z. Zhao, "Normal inverse gaussian model-based image denoising in the nsct domain," *Mathematical Problems in Engineering*, vol. 2015, 2015.
18. A. Fathi and A. R. Naghsh-Nilchi, "Efficient image denoising method based on a new adaptive wavelet packet thresholding function," *IEEE transactions on image processing*, vol. 21, no. 9, pp. 3981–3990, 2012.
19. J. Odstrcilik, R. Kolar, A. Budai, J. Hornegger, J. Jan, J. Gazarek, T. Kubena, P. Cernosek, O. Svoboda, and E. Angelopoulou, "Retinal vessel segmentation by improved matched filtering: evaluation on a new high-resolution fundus image database," *IET Image Processing*, vol. 7, no. 4, pp. 373–383, 2013.

## AUTHORS PROFILE



**Anil Kumar K. Rwas**, born in Kerala, India in May 1977. He took his B.Tech degree in Electronics Engineering with first class from Cochin University of Science and Technology (CUSAT), Kerala, India in June 1999 and M.Tech degree in Industrial Electronics from Visvesvaraya Technological University (VTU), Belgaum, Karnataka, India in September 2010 with first rank. Currently he is pursuing Ph.D degree in University of Calicut, Kerala, India. He is a life member of ISTE. Since 2000 he has been an Assistant Professor in the department of Electronics and Communication Engineering, NSS College of Engineering, Palakkad, Kerala, India. His areas of research are Biomedical Image and Signal Processing and Computer Vision.



**Dr. Meenakshy Kwas** born in Kerala, India in 1969. She received the UG degree in Electrical and Electronics Engineering (EEE) and M.Tech degree in Power Systems from Kerala University in 1990 and 1995 respectively and Ph.D degree in Biomedical Image Processing from Cochin University of Science and Technology (CUSAT) in 2011. She had been in the department of Instrumentation, CUSAT, from 1996 to 1999. Since 2000 she has been an Assistant Professor in EEE, Department of Technical Education, Government of Kerala. She has memberships in professional bodies such as IEEE, ISTE etc. Her research interests include Biomedical Image and Signal Processing, Digital Design and Embedded System Design.